J Mater Sci (2021) 56:9852–9870

Electronic materials

Fracture mechanism of microporous Ag-sintered joint in a GaN power device with Ti/Ag and Ni/Ti/Ag metallization layer at different thermo-mechanical stresses

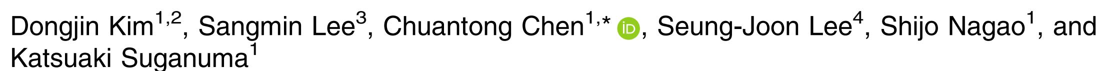

Dongjin Kim[1,2], Sangmin Lee[3], Chuantong Chen[1,*], Seung-Joon Lee[4], Shijo Nagao[1], and Katsuaki Suganuma[1]

[1] *Flexible 3D System Integration Laboratory, Osaka University, Ibaraki-shi, Osaka 567-0047, Japan*
[2] *Thermal Management Team, Production Engineering Research Institute, LG Electronics, Inc, Gangseo-gu, Seoul 07796, Republic of Korea*
[3] *Division of Materials and Manufacturing Science Engineering, Graduate School of Engineering, Osaka University, Suita-shi, Osaka 565-0871, Japan*
[4] *Department of Advanced Materials Engineering, Korea Polytechnic University, Siheung 15073, Republic of Korea*

Received: 11 November 2020
Accepted: 9 February 2021
Published online:
25 February 2021

© The Author(s), under exclusive licence to Springer Science+Business Media, LLC part of Springer Nature 2021

ABSTRACT

Ag sinter joining technology is emerging as a die attach material for next-generation power modules in high-temperature applications. Thermal shock test has revealed that the fracture characteristics and reliability of sintered Ag joint were influenced by thermo-mechanical stress. This was study conducted to understand the microstructure, vertical crack formation, and fracture behavior of sintered Ag joints which were designed with different metallization layers on a direct bonded aluminum (DBA) substrate, at different thermo-mechanical stresses during thermal shock tests. Two kinds of metallization layers were designed as Ti/Ag and Ni/Ti/Ag layers. A finite element model (FEM) simulation confirmed that the Ni layer prohibited Al hillock-like deformation and generates different thermo-mechanical stresses during the thermal shock test from − 50 °C to 250 °C. Depending on the degradation of the interfaces for both of the Ag-sintered joints, the sintered Ag grain necking thickness and microstructure characteristics including the Ag grain structures, which have a dominant influence on the bonding strength in terms of long-term reliability, are considerably different from the results by an electron back scatter diffraction (EBSD) analysis. This paper proposes a novel metallization technology that can induce joint fracture with complete recrystallization of sintered Ag joints by effectively suppressing interfacial degradation. The mechanism of this technology was systematically analyzed through experiments and FEM simulations.

Handling Editor: Kevin Jones.

Address correspondence to E-mail: chenchuantong@sanken.osaka-u.ac.jp

Springer

https://doi.org/10.1007/s10853-021-05924-z

Introduction

Silicon carbide (SiC) and gallium nitride (GaN) semiconductors offer many benefits in various industries in terms of high power efficiencies [1–5]. A power conversion system using SiC or GaN devices can be applied beyond 250 °C and withstand higher power density, enabling system volume miniaturization. In the power modules, the huge heat generated from the SiC or GaN die surface is conducted through the die attach material and the substrate and finally reaches a heat sink plate. In this case, die attach materials are a key element for the implementation of higher power and miniaturization, especially for the high-temperature applications. The development of die attach materials that can withstand the high temperature caused by a high power density is urgently required to improve the long-term reliability of power conversion systems without massive and heavy cooling systems.

In the past, Pb-, Sn-, Au-, Zn-, and Ag-based solder alloy materials were actively developed [6–8]. However, these materials have various limitations, such as environmental effects, high price, high-temperature processes, intermetallic compound (IMC) formation, poor process-ability, and brittleness [9–14]. Recently, Ag sinter joining technology represents a radical departure from previous processes because it possesses excellent thermal, electrical, and mechanical properties and a simple manufacturing process [15]. Recently, a low-temperature and low-pressure Ag sinter joining process was also developed, increasing the feasibility of actually application [16–19].

Ag sinter joining technology has been reported to cause serious degradations to interfaces owing to the coefficient of thermal expansion (CTE) mismatch in harsh environments such as thermal shock (− 50 °C/ 250 °C) or high-temperature aging [20]. Previous studies have reported that vertical cracks formed inner sintered Ag joining layer during repetitive power cycling or thermal shock cycling tests, which was one of the main features of the degradation mode [20]. In addition, to achieve a robust interface bonding, the metallization on both the chip and substrate side usually used the Ag metallization layer because the same element is present as the Ag particles, leading to a better interface bonding than other metallization layers especially in a low-temperature low-pressure sintering process. In addition, Ni is widely used as a metallization layer in power electronics, in Ni/Au, Ni/Pd/Au finishes as a diffusion barrier and some other functions to provide good solderability, for instance, to produce an intermetallic compound (IMC) Ni_3Sn_4 layer after reacting with Tin (Sn). Recently, to overcome these degradations, some studies have focused on the improvement of various metallization technologies on both the chip and substrate side and various substrates to reduce the thermo-mechanical stress and thus improve the mechanical reliability of WBG die-attached structures [21–23]. S. Noh et al. reported on the reliability of sintered Ag joining on Ag, Ni/Ag, Ti/Ag and Ni/ Pd/Pt/Ag metallized substrate during a thermal shock test [24]. The fracture characteristics and reliability of die-attached modules by Ag sinter joining technology was largely influenced by different metallization layers during a thermal shock test due to the different thermo-mechanical stress.

In our previous study [25], Ni/Ti/Ag metallization layers were designed and applied to a direct bonded aluminum (DBA) substrate, therefore prohibiting the plastic deformation of the Al layer during a thermal shock test and improving the reliability of the sintered Ag joint. The shear strength did not change significantly after 500 h thermal shock test varied from -50 to 250 °C. Compared to the case with the Ti/ Ag metallization layer, the crack formation and fracture behavior were changed in the case of Ni/Ti/ Ag metallization layer [20]. Although the different metallization layers led to different thermo-mechanical stresses during the thermal shock test, the mechanism of crack formation and the deformation behavior of sintered Ag layer are not clearly understood under different thermo-mechanical stresses. The effect of thermo-mechanical stress on the microstructure, crack formation, and fracture behaviors of sintered Ag joint structure is one of the most important issues because it correlates with the lifetime of the die-attached power module.

In this study, two different metallization layers, Ni/Ti/Ag and Ti/Ag, were sputter-coated on DBA substrates in a GaN power module joined using Ag sinter joining technology. The GaN die-attached structures were implemented into a thermal shock test from − 50 to 250 °C. The thermo-mechanical stress and thermal flux in the two cases were analyzed using a finite element method (FEM) simulation. The thermo-mechanical stress effects on the grain structures of the sintered Ag layer,

metallization layers, and Al (DBA) substrate layer during the thermal shock test were systemically investigated by electron backscatter diffraction (EBSD), scanning electron microscope (SEM), and energy-dispersive spectroscopy (EDS) analysis. In addition, the mechanism of crack formation of sintered Ag layer, fracture characteristics of the GaN die-attached structure, which correlates with experimental results, are proposed based on the other FEM simulation.

Materials and methods

Specimen preparation

Hybrid Ag paste, which displays submicron Ag particles and micron-scaled Ag flake particles, as shown in Fig. 1a and b, respectively, was used in this study. The Ag submicron particles (FHD, Mitsui Mining and Smelting Co., Ltd, Japan) and micron-sized Ag flakes (AgC239, Fukuda Metal Foil and Powder, Kyoto, Japan) were mixed as Ag fillers in a weight ratio of 1:1 [26]. GaN dies with the dimensions of 5 mm × 5 mm × 0.5 mm were introduced to bond with the DBA substrates (Al/AlN/Al) which have a dimension of 30 mm × 30 mm × 1.23 mm. Figure 1c shows a GaN/DBA die-attached structure and its depiction of each metallization layer. In the case of Ti/Ag metallization layers, 200 nm Ti and 2 μm Ag were orderly sputtered on the back side of the GaN die and top side of the DBA substrate. In the case of Ni/Ti/Ag metallization layers, 200 nm Ti and 2 μm Ag were sputtered on the back side of the GaN die, and 7 μm Ni, 200 nm Ti, and 2 μm Ag were sputtered on the top side of the DBA substrates. Ag paste was printed on the DBA substrate by a metal mask which has a thickness of 100 μm. After printing the hybrid Ag paste on the metallized DBA substrates with and without Ni, GaN die was mounted onto the Ag paste by hand operation. Pressure-less sintering was realized using a temperature profile of 250 °C for 30 min in air. The detailed sintering process can be found in our previous study [26]. After the sintering process, the sintered Ag layer has a micron-sized porous network structure [26].

Thermal shock tests and evaluations

Thermal shock test was conducted using a thermal shock chamber (TSE-11-A-S, ESPEC, Osaka, Japan). The evolution of the microstructures and mechanical properties were investigated before and after thermal shock test. Thermal shock test was conducted at temperatures ranging from − 50 °C to 250 °C, and the dwell time is 30 min at − 50 °C and 250 °C for each cycle (see Fig. 1d). The specimens subjected to the thermal shock cycle test were then shear tested using a shear tester machine (DAGE 4000 bonds tester, UK) at a speed of 50 μm/s (see Fig. 1e). The cross section of the sintered Ag joint was prepared by an ion-milling polishing machine (IM4000, Hitachi, Tokyo, Japan), and the microstructural characteristics were observed by field-emission scanning electron microscopy (FE-SEM, SU8020, Hitachi, Tokyo, Japan), energy-dispersive X-ray spectroscopy (EDX), and electron backscatter diffraction (EBSD; EDAX-TSL, Hikari).

Microstructural information such as statistical distributions of grain size, misorientation angle, and Σ3 twin boundary was obtained by TSL-OIM analysis software Ver. 4 after EBSD observation. The operation voltage of the SEM was 15 kV. The points with confidence index (CI) less than 0.1 were excluded in this analysis. The KAM data included the nearest neighbor grain pixels was obtained by Hough-based EBSD in order to quantify the intragranular misorientation. In addition, for quantitative microstructure analysis, both EBSD detection and KAM analysis for all the specimens were scanned under the same conditions.

Numerical simulation models

Finite element method (FEM) simulations were performed to understand the thermo-mechanical stress and thermal behavior inside the sintered Ag joint structure and to investigate the mechanical response of the degraded interface during the shear tests. For this work, ANSYS workbench R19.2, a commercial finite element analysis (FEA) program, was introduced for the FEM simulation, and the thermal–mechanical behavior was solved. The thermal conductivity coefficient (k) was assumed as isotropic and calculated by the Fourier's thermal conductivity Eq. (1) as follows:

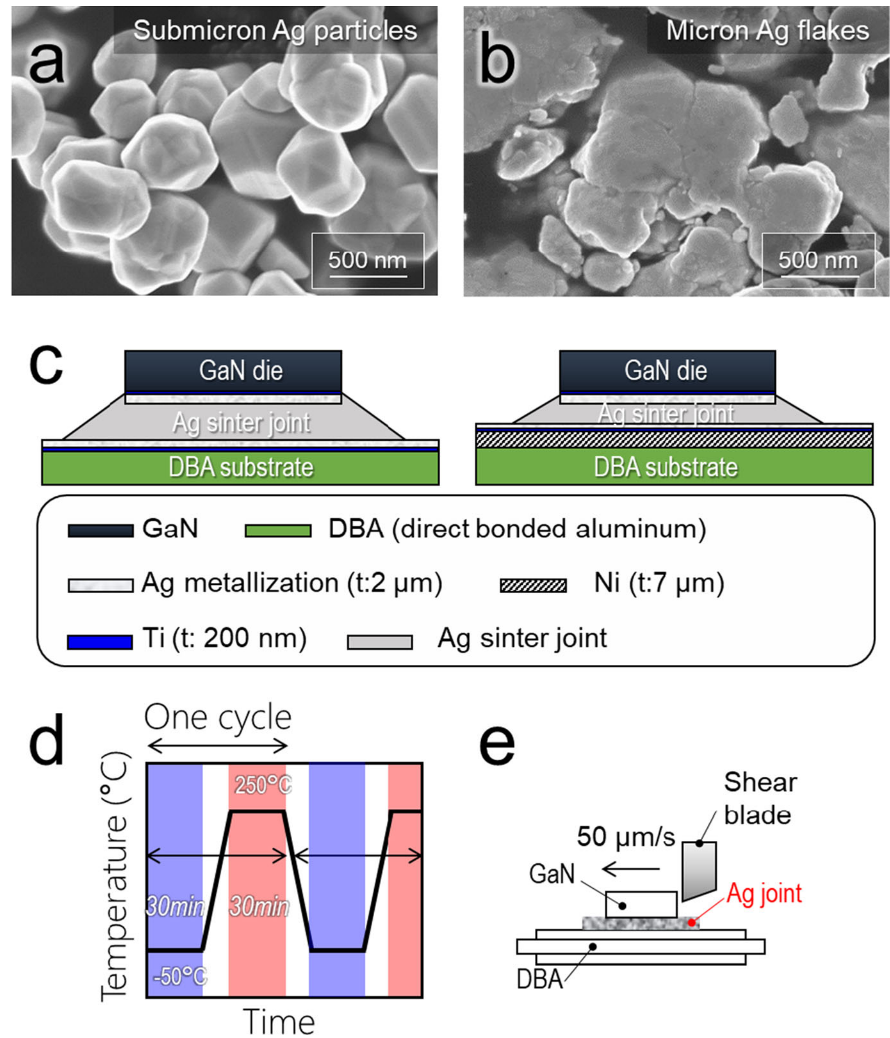

Figure 1 Ag particles, Ag flakes, cross sections, and bonding strength: **a** submicron Ag particles, **b** micron Ag flakes, **c** schematic description of GaN die-attached structures, and **d** thermal shock cycling test condition, **e** schematic description of a die shear test condition after thermal shock cycling test.

$$\frac{\partial T^2}{\partial x^2} + \frac{\partial T^2}{\partial y^2} + \frac{\dot{e}_{gen}}{k} = \frac{1}{a}\frac{\partial T}{\partial t} \tag{1}$$

Then,

$$a = \frac{k}{\rho c} \tag{2}$$

where a is a thermal diffusivity, c is a specific heat, and ρ is a density of material. The FEM simulation and boundary conditions used to determine the stress mechanism are shown in Fig. 2. Because the shape of the pore is difficult to specify in the FEM simulation, all the pores were described as a circle shape. In addition, to ensure the pore size was close to the actually Ag-sintered joint in FEM simulation, which were set as a range from 1 to 3 μm in FEM simulation. Figure 2a and b exhibits the 2D-FE modeling of the GaN-DBA die-attached structure without the Ni metallization and with the Ni metallization by Ag sinter joining, respectively. Steady-state and transient-thermal conditions were coupled to simulate the change of thermal behavior during the cooling process as shown in Fig. 2c. After the unsteady thermal analysis, the static structural solver applied to calculate the mechanical response to thermal shock with the temperature change of 300 °C. The approach was taken to simulate the 3-D porous material with a 2-D geometry. This could introduce errors which can be quantified by calculating the effective thermal conductivity of the porous material in the simulation and comparing with the actual measured thermal conductivity of the porous Ag with the same volume fraction of pores. The difference between the two values should be presented so that the size of the errors can be estimated. To minimize and implement effectively this issue, the properties of the porous Ag-sintered layer applied in this study are the physical/

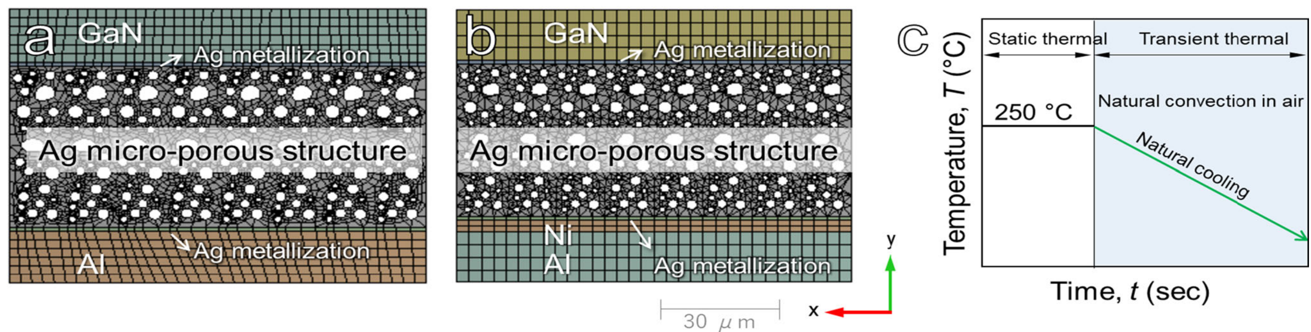

Figure 2 Finite element method (FEM) simulation conditions for the thermal stress behavior. **a** FE modeling of the DBA substrate without the Ni specimen, **b** FE modeling of the DBA substrate with the Ni specimen, and (**c**) the temperature condition.

mechanical properties that were measured and applied to simulations reported in previous studies [27–29]; the material properties used in the FEM calculation are listed in Table 1.

Results

Microstructure evolution of Ag-sintered joints

SEM cross section

Initial state of die-attached structures without a Ni metallization layer and with a Ni metallization layer are shown in Fig. 3a and b, respectively. Both cases show structurally sound well-bonded as-sintered state, and the sintered Ag layer exhibits a microporous structure. In this study, the image processing software IPWIN32 was applied to calculate the porosity. The porosity of initial as-sintered joints without Ni metallization layer was measured as 55% and was measured as 56% for the Ni metallization layer case. The thickness of sintered Ag layer was about 30 μm for the joint without Ni metallization and was about 20 μm for the joint with Ni metallization. The difference in the thicknesses can be attributed to the chip mounting process, where the GaN die was mounted onto the Ag paste by hand operation after printing the Ag paste on the metallized DBA substrates. The thickness of sintered Ag can be considered as a normal fluctuation during the experiment. In addition, because Ag paste have the same thickness of 100 μm, the fluctuation of sintered Ag layer must be within a reasonable range. Therefore, the difference in the thicknesses of the sintered Ag layer should have a very small effect on the shear strength and evolution during thermal cycling. Figure 4 shows scanning electron microscope (SEM) cross section images of the die-attached structures without a Ni metallization layer and with a Ni metallization layer after thermal shock cycles. In the case of the GaN die-attached structures without Ni metallization layer, vertical direction cracks were generated inside the sintered Ag layer from 125 cycles. Furthermore, considerable deformation of the Al layer can be observed after 125 cycles. The vertical cracking initiation inside the sintered Ag joint may be induced by generation of the Al hillock-like structures, as shown in Fig. 4a. After 500 cycles, the vertical direction cracks became more significant as the

Table 1 Material properties for the FEM calculation

	Density (kg/m^3)	Thermal conductivity (Wm^{-1} K^{-1})	CTE (K^{-1})	Elastic modulus (GPa)	Yield stress (MPa)	Poisson ratio (%)
GaN	6100	110	5.6×10^{-6}	181	–	0.352
Ag-sintered joint [27–29]	6924	430	21.1×10^{-6}	16.7	13.8	0.31
Al	2700	137	25.7×10^{-6}	70	100	0.33
Ni	8900	90.7	13.4×10^{-6}	200	–	0.31

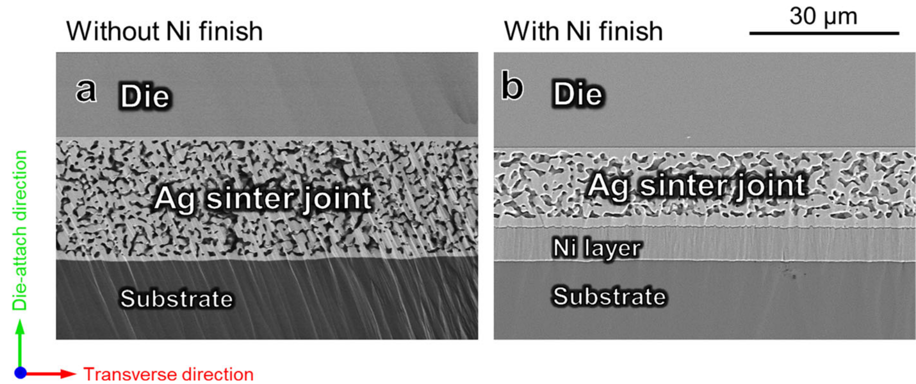

Figure 3 Cross-sectional image of initial state specimens. **a** Ag-sintered joint structure without Ni finish and **b** Ag-sintered joint structure with Ni finish.

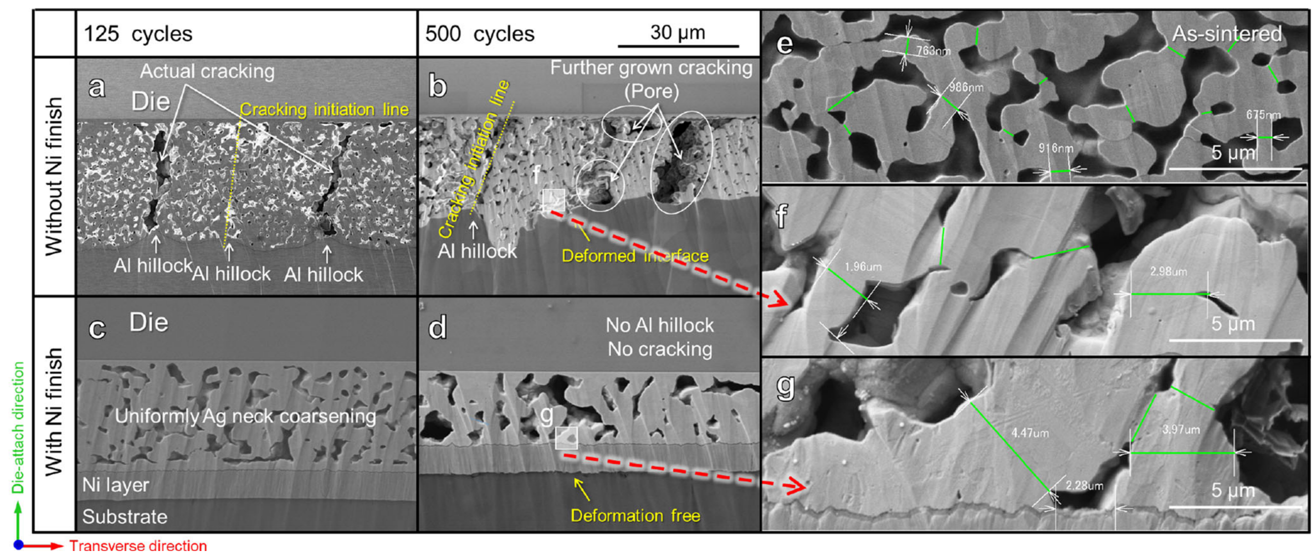

Figure 4 Cross-sectional image of Ag-sintered joint after thermal shock test. **a** SEM image of a degraded specimen without a Ni finish after 125 cycles and **b** 500 cycles; **c** SEM image of a degraded specimen with a Ni finish after 125 cycles and (**d**) 500 cycles; **e** necking thickness of the as-sintered Ag, **f** necking thickness change in the case of joint without Ni metallization; and (**g**) in the case of joint with Ni metallization.

necking of the sintered Ag joint increased, and the Ag–Al interface changed more heterogeneously beyond the deformation and size of the Al hillock-like structures, as shown in Fig. 4b.

On the other hand, in the case of the GaN die-attached structures with Ni metallization, the increase of the necking thickness of the sintered Ag joint was uniform. In addition, Al hillock-like deformation or major defects could not been observed after 125 cycles or even after 500 cycles (see Fig. 4c, d). Here, the necking thickness represents the degree of inter-diffusion of Ag grains. The necking thickness of the as-sintered Ag layer is shown in Fig. 4e. Figure 4f and g shows the magnified view of the sintered Ag layer after 500 cycles for the Ag-sintered joint without and with the Ni metallization layer, respectively. The necking thickness of sintered Ag layer is marked in Fig. 4f and g. Therefore, it can be suggested that the growth of Ag necking thickness and Al hillock-like deformation were largely related to the vertical direction cracks formation of sintered Ag joint. The main features related to the necking thickness growth of the sintered Ag joint are discussed in detail in the next section.

Pore size and necking thickness

The pore size and grain necking thickness of the sintered Ag layer were measured using SEM utility software of IPWIN 32 before and after the thermal shock test. In addition, the average diameter of the pore size was calculated by the pores area divided by

the pores number based on the SEM image. Figure 5 shows the measurement results of the average pore size and grain necking thickness of the microporous sintered Ag joint before and after the thermal shock test. In the case of the joint without Ni metallization, if we do not consider the cracks generated inside the Ag-sintered joint, the pore size of the sintered Ag layer increased from 2.0 μm of as-sintered state to 3.1 μm after 125 cycles with cracking initiation, and to 3.9 μm after 500 cycles. This case showed that the pore size from 125 cycles of thermal shock is almost saturated and remains at a similar thickness up to 500 cycles. In addition, the pore size increased quickly if all the cracks were accounted as the pore area as shown in Fig. 5. In contrast, in the case of the joints with Ni metallization, the pore size of sintered Ag particles layer increased from the initial 2.0 μm to 5.2 μm after 125 cycles, and to 5.8 μm after 500 cycles. It can be estimated from these results that vertical direction cracks generation inside the sintered Ag layer may prohibit the Ag atom from moving, leading to a relatively slow pore size coarsening. This result is further discussed in discussion section in detail. In addition, the necking thickness of the sintered Ag layer was influenced by the different metallization layers, as shown in Fig. 5b. With Ni metallization, the necking thickness of sinter Ag joint doubles compared to the case without Ni metallization case.

Grain structure characteristics analysis by EBSD

Ag-sintered joints EBSD analysis was performed to understand the change in the internal grain structure of the sintered Ag particles layer before and after the thermal shock tests, as shown in Fig. 6. For the microporous Ag structures, the scanning area and step size of EBSD in the Kikuchi pattern scanning were 75 μm × 75 μm and 25 nm. About 20 grains were taken into accounted for EBSD analysis for each specimen. In the as-sintered Ag layer, grain orientations were randomly distributed with IPF map analysis as shown in Fig. 6a. Figure 6b exhibits the IQ map where the low angle grain boundaries (LAGBs, $2° < \theta < 15°$) are marked by a green line, the high angle grain boundaries (HAGBs, $15° < \theta$) are marked by a blue line, and the $\sum 3$ boundaries are marked by a red line. The kernel average grain misorientation (KAM) maps in Fig. 6c are drawn by an average grain misorientation angle with a maximum angle of 3°.

For the case of joints without the Ni metallization layer on the DBA substrate, the grain orientation was randomly distributed after 500 thermal shock cycles as shown in Fig. 6d. It can be seen that the fraction of LAGBs decreases significantly, as shown in Fig. 6e, compared with the as-sintered Ag particles layer. The KAM value after the thermal shock tests was lower than that the initial state, indicating that the initial dislocation of high energy from LAGBs was released

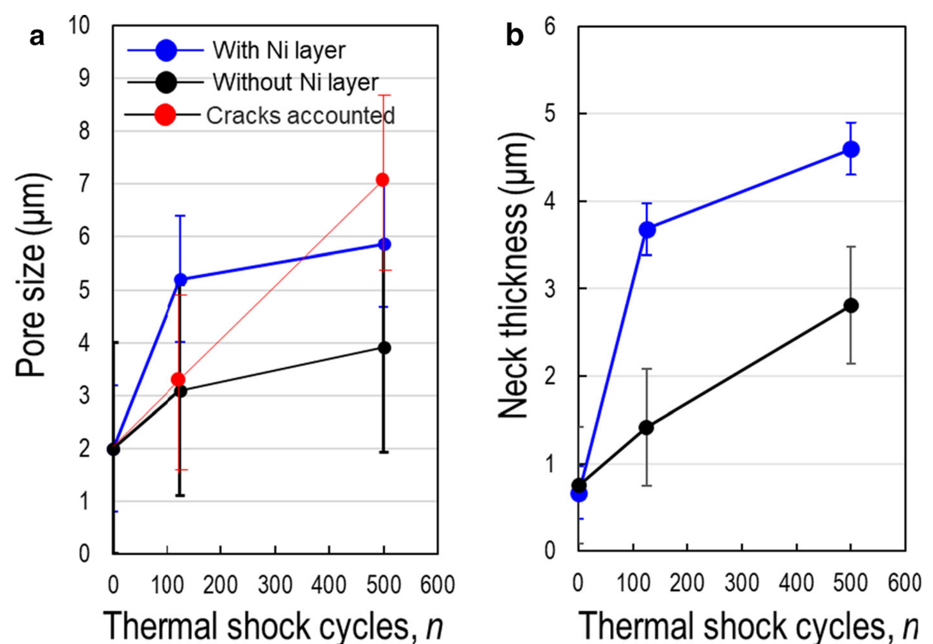

Figure 5 **a** Pore size change after thermal shock test for both joint with Ni and without Ni, and the case of cracks accounted for the case of joint without Ni and (**b**) necking thickness change of Ag-sintered layer after thermal shock test.

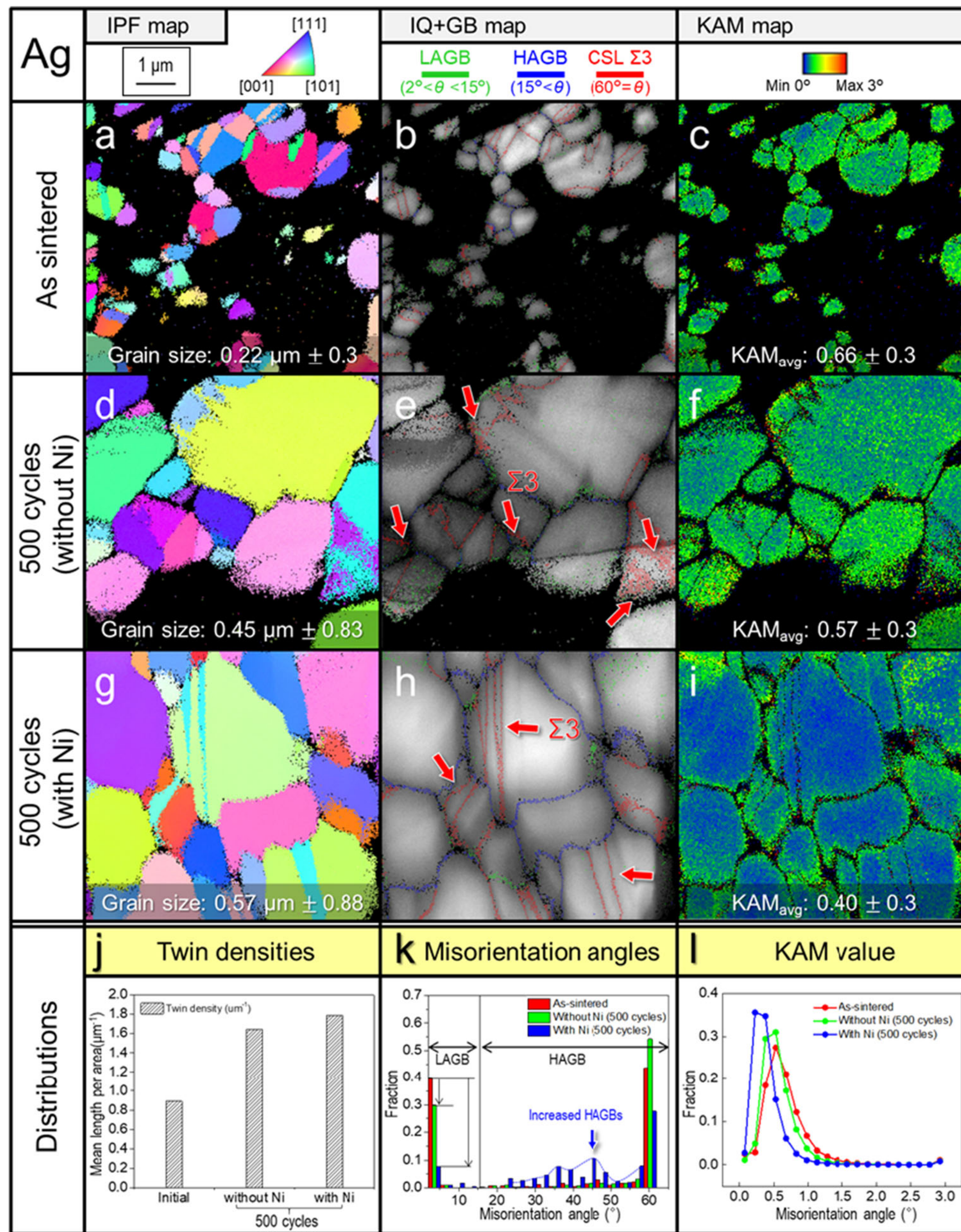

Figure 6 EBSD observation results of Ni metallization-dependent Ag-sintered joints before and after the thermal shock cycling test. **a** IPF map of as-sintered Ag joint, **b** IQ and GB map of as-sintered Ag joint, and its KAM map (**c**), **d** IPF map of Ag-sintered joint without Ni metallization after 500 cycles; **e** IQ and GB map of Ag-sintered joint without Ni metallization after 500 cycles, and its KAM map (**f**), (**g**) IPF map of Ag-sintered joint with Ni metallization after 500 cycles, **h** IQ and GB map of Ag-sintered joint with Ni metallization after 500 cycles, its KAM map (**i**), and (**j**) fraction of twin densities, **k** misorientation distributions, and kernel average misorientation angle distributions. The green lines represent the low-angle boundaries with misorientation angles between 2° and 15°, the blue lines denote high-angle boundaries with misorientation angles exceeding 15°, and the red line denote \sum 3 boundary. EBSD, electron back scatter diffraction; IQ, image quality; GB, grain boundary; KAM, kernel average misorientation.

during the process of the grain recrystallization of sintered Ag layer where the fraction of LAGBs decreased and HAGBs increased significantly (see Fig. 6f). On the other hand, the grain orientation was randomly distributed for the joint with Ni metallization layer, as shown in Fig. 6g. In particular, it had a lower LAGBs fraction and a higher overall distribution of HAGBs than that the DBA substrate

without Ni metallization layer (see Fig. 6h). As the fraction of HAGB increased significantly, the KAM value of the recrystallized Ag grain was approximately 50% lower than that the initial state (see Fig. 6i). In addition, the average grain size of the initial sintered Ag layer was 0.22 μm, which grew for both cases with and without Ni metallization layer, where the average grain size was 0.45 μm and 0.57 μm, respectively. Both of the values after the thermal shock test are more than twice as large as the value of the initial state. In addition, the average grain size of sintered Ag layer with the Ni metallization layer was slightly larger than that without Ni metallization layer. The reason will be discussed in next section by analysis of Ag atom diffusion in the both cases during the thermal shock test.

Furthermore, the grain boundaries change, including the twin boundaries, and the misorientation angle for both cases joints with and without the Ni metallization layer on the DBA substrate were also investigated and analyzed. The twin boundary density was remarkably higher than that in the initial state for both cases after the thermal shock test, as shown in Fig. 6j. Twin boundary density is expressed in length per unit area. In this study, it means the value of the selected 20 grains for each specimen. In addition, in the case of Ni finish it has a slightly higher density of twin boundary than that without Ni finish. The reasons may be attributed to the different stress distributions during the thermal shock test for the two joints, and will be further studied in our future work with more data analysis. The quantitative distribution related to these misorientation angles and KAM are displayed in Fig. 6k and l, respectively. This characteristic behavior of the grain structure for the case of joint with the Ni metallization layer was due to Al deformation was suppressed at the bonding interface during the thermal shock test. The thermo-mechanical stress from the interface does not dissipate and is uniformly transferred to the sintered Ag layer in the case with Ni metallization layer, leading to more active recrystallization than that of the die-attached structure without Ni metallization.

Al of DBA layers In addition, EBSD observation was conducted on the top part of Al (DBA) substrate as shown in a schematic sketch of Fig. 7a. In the initial state, the Al layer appeared as almost a single crystal structure with the grain orientation of [001] and shows a relatively low value of KAM with sub-grain boundaries. However, the orientations of Al show a dramatically different distribution depending on the presence or absence of Ni metallization after 500 thermal shock cycles as displayed in Fig. 7b. In the case of joints without Ni metallization, interfacial deformation between Ag and Al interface was observed as shown in the SEM image of Fig. 4, which changed the orientation of Al to colors close to yellow and promoted regeneration of many sub-grains. In particular, since relatively strong KAM values were measured in the sub-grains, it can be interpreted that Al has a high KAM value in the sub-grains by allowing plastic deformation. Conversely, in the case of joints with Ni metallization, an orientation [001] distribution after 500 thermal shock cycles was almost same as the initial state. The mean length per unit area of high-angle boundaries (HAB) is shown in Fig. 7c. Comparing with the initial state, the value of HAB largely increased after 500 thermal shock cycling in the case with Ni metallization layer, which is also larger than that without Ni metallization layer after the same thermal shock cycling. The results indicated that thermal stress will mainly promote the sub-grains generation and HAB evolution in the case of the joints with Ni metallization layer.

Ni metallization layers before and after thermal shock tests Because the Ni layer plays an important role on the thermal shock resistance, the grain structure of Ni metallization layer was further investigated before and after thermal shock.

Figure 8a exhibits a back-scattered electron (BSE) image of joint structure to explain on the appearance of the Ni metallization layer area before and after thermal shock cycling tests. Figure 8b shows the IPF and KAM value of the Ni metallization layer in initial state and after 500 thermal shock cycles. The average grain size of Ni metallization layer slightly increased from the initial 0.6 μm to 0.7 μm after 500 thermal shock cycles, and the KAM value decreased from the initial 0.68 μm to 0.6 μm. The slight change may be attributed to the thermo-mechanical stress during the thermal shock test. In addition, there was no noticeable change in grain orientation which was randomly distributed before and after the thermal shock test as shown in Fig. 8b.

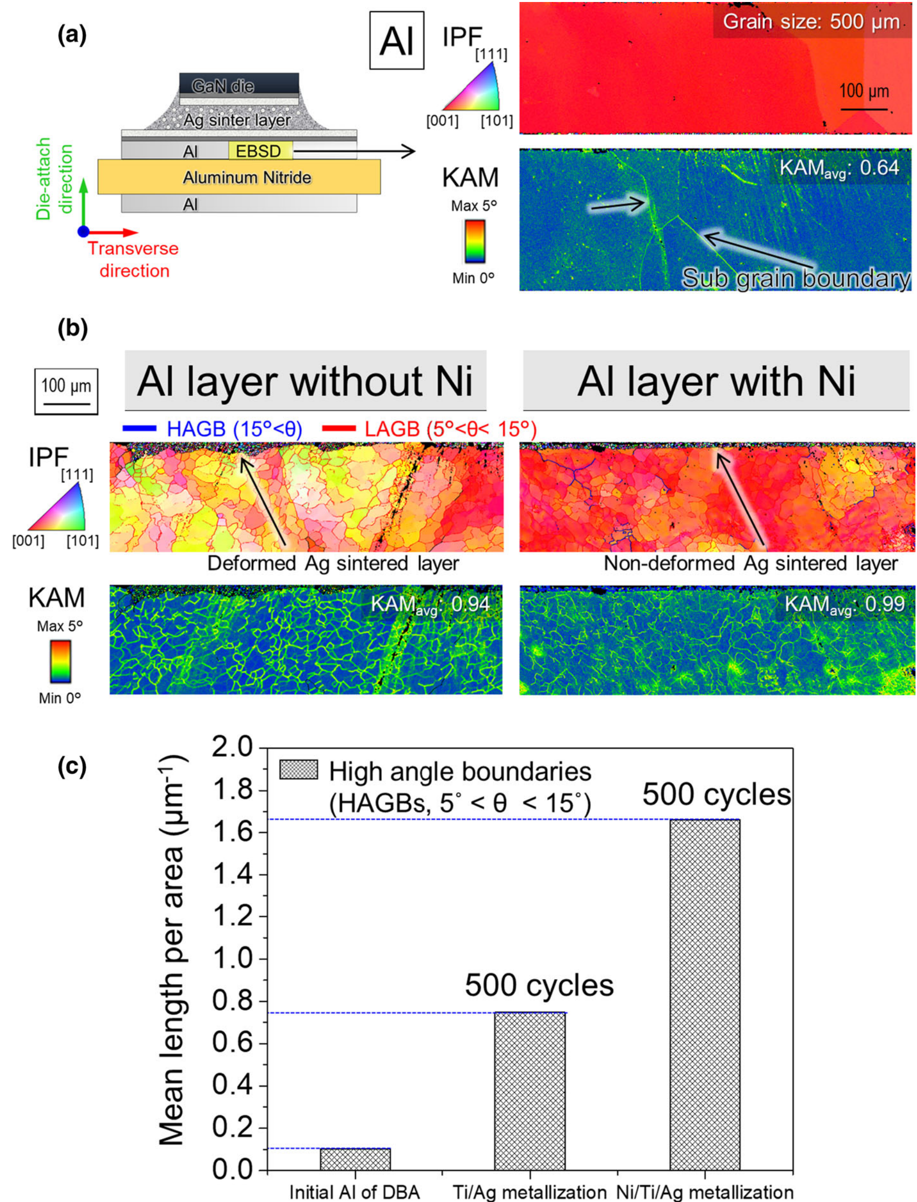

Figure 7 **a** initial state of grain structure of IPF and KAM of Al (DBA) substrate by EBSD analysis, **b** the EBSD analysis results of Al substrate after 500 thermal shock cycles for the Ag-sintered joint with and without Ni metallization layer, **c** the mean length per unit area of high-angle boundaries (HAB) for the Ag-sintered joint with and without Ni metallization layer by EBSD analysis.

Mechanical characteristics

Grain size and pore size influence

Figure 9 shows the die shear strength before and after the thermal shock cycle tests for both cases with and without Ni metallization layer. In the case of the DBA metallized by Ni/Ti/Ag, there was no substantial strength reduction after 500 cycles, but the shear strength was approximately 72% of the initial strength for the case of Ti/Ag metallization. Because there are very few reports about the materials properties of porous Ag related with its grain structure, in this study, the possible relationship between the shear strength of Ag-sintered joint structure and its grain structure is discussed. In both joints with and without Ni metallization layer, the shear strength decreased as the grain size gradually increased as shown in Fig. 9. It is noteworthy that the Ag-sintered joint structure with Ni metallization layer tended to follow the typical Hall–Petch relationship by the values before and after thermal shock 125 and 500 cycles. The Hall–Petch law is well known where the strength of a polycrystalline material increases with decreasing grain size [30]. In general, the Hall–Petch relates the material's yield strength with its grain size where a smaller grain size would produce a higher

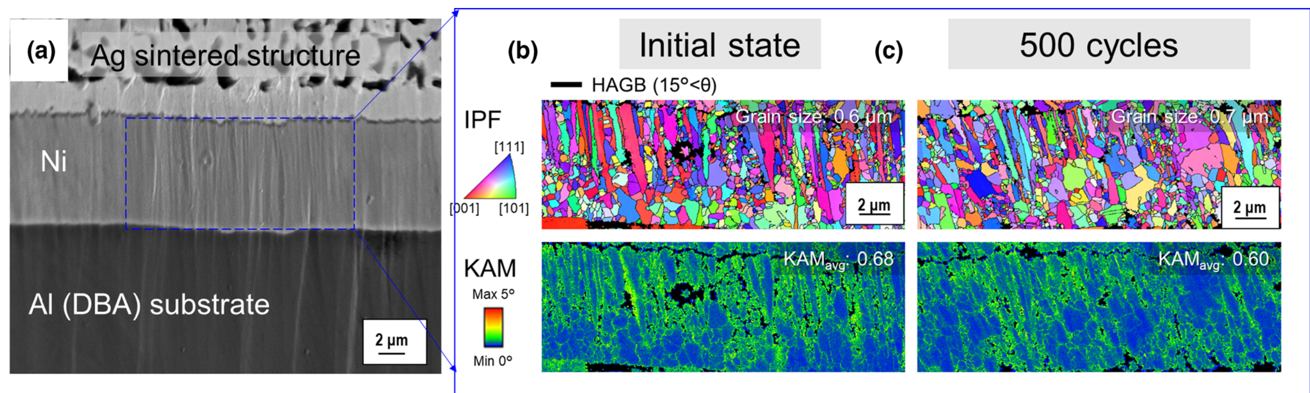

Figure 8 **a** the BSE image of the Ag-sintered joint at the bonding interface of Al substrate, (**b**) the IPF and KAM results of Ni metallization layers (**b**) before and (**c**) after 500 thermal shock cycling tests by EBSD analysis.

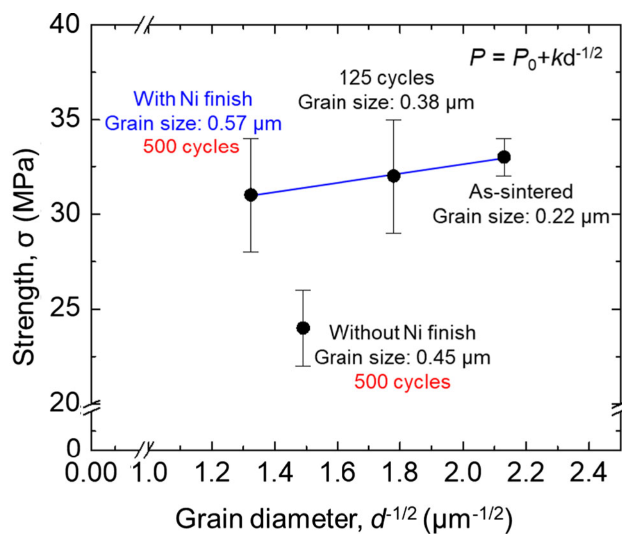

Figure 9 Shear strength of Ag-sintered joint before and after thermal shock test related with the Ag grain size change.

yield strength. Some studies also pointed out that because the maximum shear stress is a failure theory that is regarded as the criterion for yield generation, shear stress can be expressed as a function of yield stress [31]. Therefore, the grain size of Ag-sintered joint structure with Ni metallization layer may directly influence the shear strength for the Ag-sintered joint structure. In addition, for the Ag-sintered joint without Ni metallization layer, the values just before and after 500 thermal shock cycles were provided. The relationship between shear strength and the Ag grain size for this case will be further studied in our future work with more data analysis.

On the other hand, previous work has reported that pore size also directly affects the stress distribution of the Ag-sintered joint by a FEM simulation analysis [32]. As analyzed in Figs. 4 and 5, the pore size changes due to coarsening, and grain structure evolution for both the Ag-sintered joints with and without Ni metallization was largely different. The different pore size may be one of the reasons of the shear strength difference. In addition, due to the vertical cracking generation induced by the hillock-like deformation of Al layer for the case without Ni metallization layer, the shear stress may be much more concentrated at the cracks locations, leading to facture mode change and shear strength decrease. Therefore, the thermal shock reliability of sintered Ag porous structure is a combination of grain structure, pore size coarsening and vertical cracking generation, which should largely depend on the thermo-mechanical stresses during the thermal shock test.

Fracture surface analysis

These different microstructural evolutions and mechanical strength evolutions substantially affect the fracture mode change. Figure 10 shows the results of fracture surface analysis and EDX analysis results for both cases with and without a Ni metallization layer after 500 thermal shock cycles. The shear force direction was marked in the figure. In Fig. 10a, the surface was very non-uniformly fractured, and the EDX analysis revealed that peaks can distinguish two very different materials, i.e., Ag and Al elements. Even the Al-detected part clearly exhibited a severely deformed hillock, and the thin Ti barrier was considered damaged by the severe deformation of Al. Figure 10b exhibits the fracture surface of Ag-sintered joint without Ni metallization layer. The fracture occurred at the Ag–Al interface,

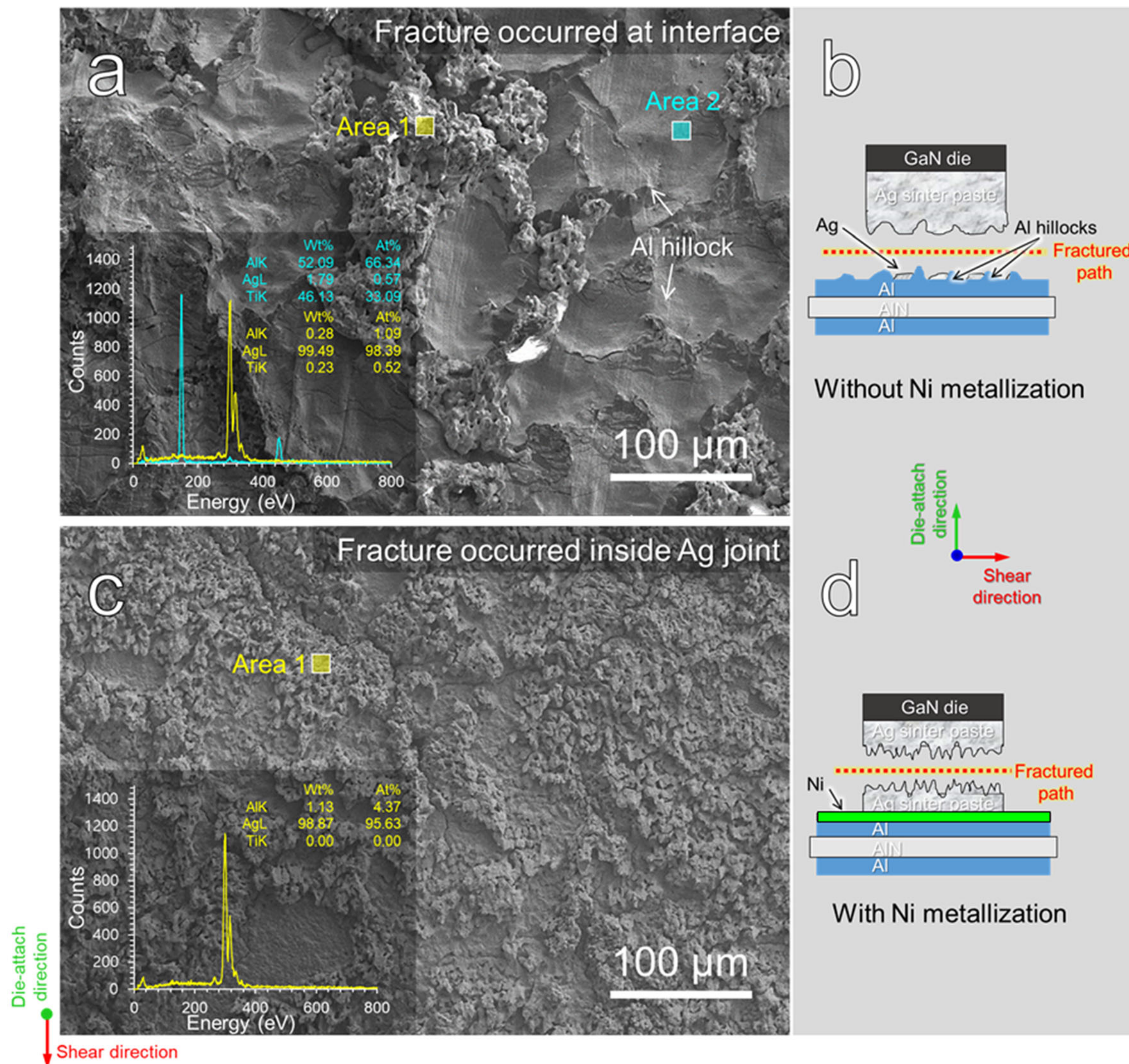

Figure 10 **a** Fractured surface and EDX element analysis of sintered Ag joint without the Ni metallization where fracture occurred inside the Ag joint, **b** schematic description of fracture path of (**a**) and (**c**) fractured surface and EDX element analysis with the Ni metallization where the fracture occurred at the interface, **d** schematic description of fracture path of (**c**).

and the loads probably concentrated at non-uniform geometric discontinuities during fracture. However, in the case of joint with Ni metallization layer, the fracture surface exhibited a completely different fracture surface morphology and EDX analysis results. The EDX analysis revealed only Ag peaks as shown in Fig. 10c, indicating that fracture occurred inside the sintered Ag layer as shown in Fig. 10d. Consequently, as can be seen from the remarkable difference in the fracture mode after thermal shock tests, in the specimen without sputtered 7 μm Ni finish, the Ag-sintered layer–Al interface was severely damaged, and the load from the shear test was concentrated at geometrically uneven area, leading to fracture easily. In this fracture behavior, it is further discussed in the fracture mode simulation section in detail.

In addition, the stress–strain curve can distinguish whether a material behavior is brittle or ductile and is important to evaluate the fracture behavior of the Ag-sintered joint. As seen in Fig. 10, the difference in failure mode was obviously revealed, and the stress–strain curve responses were well with the fracture surface analysis. Figure 11 shows the representative stress–strain curve of sintered Ag joint after 500 thermal shock cycles. Both of the stress–strain curves of sintered Ag joint with and without Ni metallization were increased during the shear test. Based on

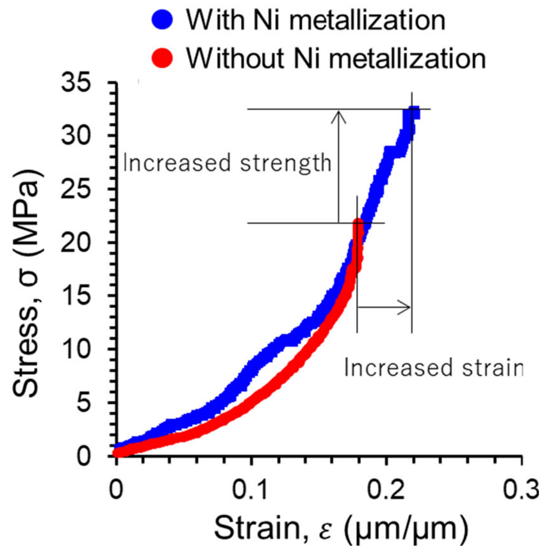

Figure 11 Shear stress-shear strain curve of sintered Ag-sintered joint with Ni and without Ni metallization from shear tests after 500 thermal shock cycles.

the results of the microstructure and grain structure of sintered Ag joint, this stress–strain curve is evidence that the Ni metallization plays a role in significantly increasing the fracture strength and ductility of the Ag-sintered joint.

Thermal stress and fracture mode analysis by FEM simulation

Thermal stress analysis

To understand the different metallization layers and their effect on the shear strength, microstructure evolution, and grain structure of the Ag-sintered joint, FEM analysis was performed in both cases with and without a Ni metallization layer during a thermal shock test. Figure 12 shows the thermal and mechanical responses for the substrates under transient-thermal conditions. To investigate the effect of Ni metallization layer on the stress and strain distribution, the three representative nodes were selected. One node was near to the GaN chip (Node 3), the other one was selected at the center of the joint (Node 2), and the third one was near the DBA substrate (Node 1). In this study, σ_{yy} was determined as an evaluation component of the stress to evaluate the crack behavior in the vertical direction. Here, σ_{xx} is a transverse stress component. The vertical direction stress (σ_{yy}) distribution of the die-attached structure without Ni metallization layer is shown in Fig. 12a. The distribution of non-uniform stress appeared at the interface between the sintered Ag layer and the Al (DBA) substrate. In addition, the non-uniform stress distribution was similar to the trace of Al hillocks-like deformation. The heat flux behavior is shown in Fig. 12b, where the temperature of 250 °C was applied to the sintered Ag layer. Heat flux (Φ) can be defined as the rate of heat energy transfer through a given surface (W), and the heat flux density (φ) is the heat flux per unit area (W/m^2). The gradient of heat flux was more than three times different among the selected nodes, which directly affected the stress behavior (see Fig. 12c). Micro-cracks are considered to be caused by this stress gradient, and it is assumed that their initiation and propagation occurs in the non-uniform section, such as hillock-like deformation.

On the other hand, the FE model with the Ni metallization layer showed a relatively uniform stress distribution without a thermal flux gradient (see Fig. 12d). The stress mainly concentrated at the Al (DBA) layer under the Ni metallization layer because the Ni metallization layer prevented the Al layer deformation during the thermal shock test. In addition, the heat flux gradients values were significantly lower than that without the Ni metallization layer case as displayed in Fig. 12e. This heat flux gradient also directly affects the stress behavior, and its peak is two times lower than that of the case without the Ni metallization layer (see Fig. 12f). Thus, uniform thermo-mechanical behavior did not cause noticeable thermal and stress effects at the interface during harsh thermal shock cycles. It has been numerically found that different surface finishes can cause different vertical stress distributions in the Ag-sintered joint.

Fracture mode simulation

To further understand the reason for the strength reduction of the interface condition due to the difference in surface finish during the shear tests, the other FEM simulation was performed. FE modeling (see Fig. 13a–c) was performed based on actual SEM cross-sectional images, as shown in Fig. 4(b, d), to reveal how the degraded die-attached structure affects the shear strength reduction. Elasto-plastic analysis was implemented in the FEM simulation, where the sintered Ag layer was assumed as an elasto-plastic material, and the values of the elastic

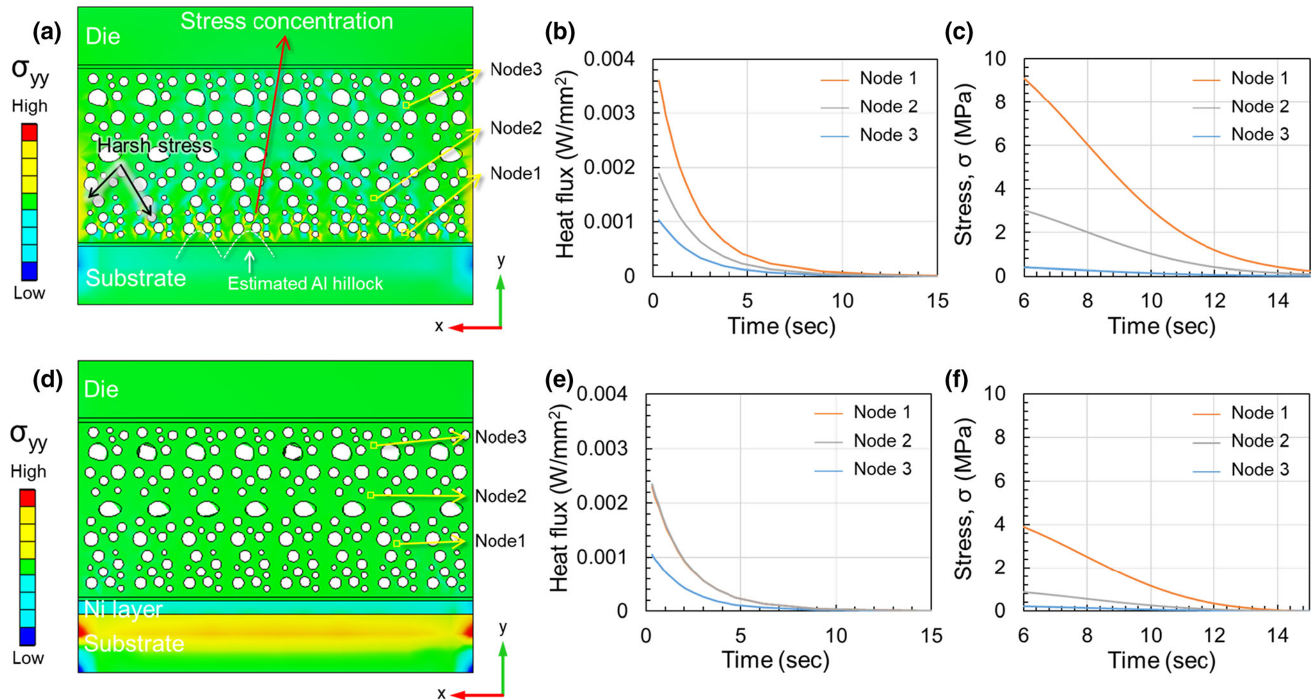

Figure 12 Thermal stress calculation of the DBA substrates without and with the Ni finish by FEM: **a** σ_{yy} distribution of the die-attach substrates of the FE model without the Ni finish, **b** transient heat flux result during the cooling process, and (**c**) its stress intensity at specific nodes; **d** σ_{yy} distribution of the die-attach substrates of the FE model with the Ni finish model, **e** transient heat flux result during the cooling process, and (**f**) its stress intensity at the selected specific nodes.

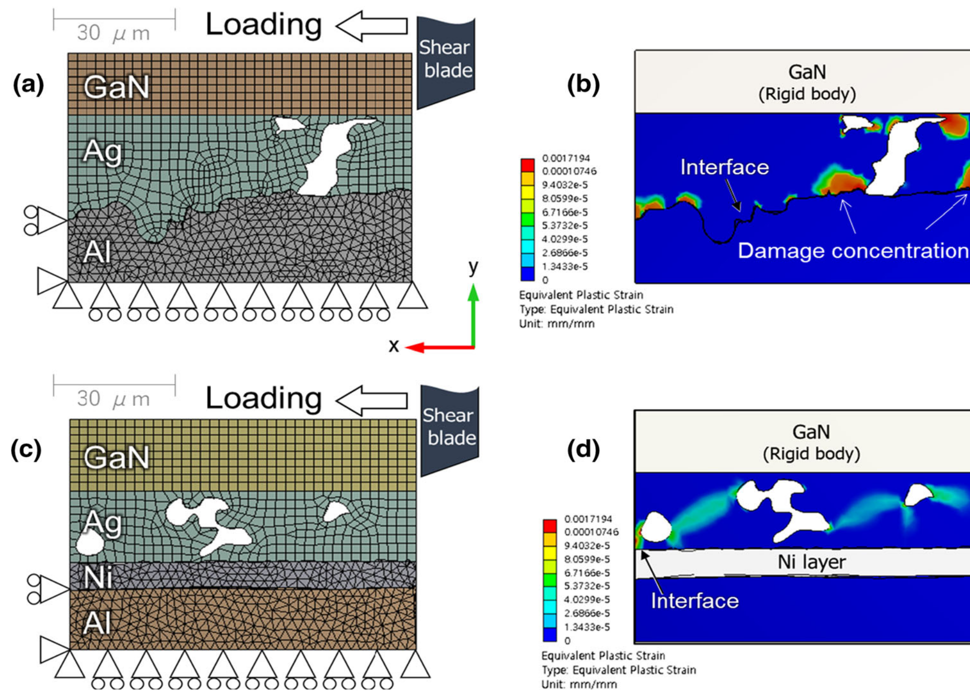

Figure 13 FEM simulation results of the shear test. **a** SEM image-based FE modeling and boundary conditions without the Ni layer, plastic strain distribution (**b**); **c** SEM image-based FE modeling and boundary conditions with the Ni layer, and plastic strain distribution (**d**).

modulus, Poisson ratio, and yielding stress were 16.7 GPa, 0.31, and 13.8 MPa, respectively [29]. Figure 13b shows the plastic strain (ε_p) distribution of the specimen without Ni metallization during the shear loading process. The intensity of the plastic strain is mainly concentrated around the Ag–Al interface, suggesting that fracture easily occurs at this Ag–Al interface part. On the order hand, as seen in Fig. 13d, the plastic deformation occurred relatively weakly inside the sintered Ag layer, and the plastic strain was not concentrated at the interface, which is consistent with the fracture surface confirmed by the actual experiment results (see Fig. 10). Previous study also reported that fracture may have occurred with a cohesive zone model by finite element analysis to predict the fracture at interface [41]. Implementing the simulation of fracture behavior from this point of view will be covered in further detail in the future works.

Discussions

Vertical crack mechanism

Vertical crack is a major degradation mode in Ag sinter joining technologies during thermal shock cycling and power cycling tests. Therefore, understanding the mechanism of crack formation can provide a decisive key for prevention of the failure. In this study, based on the experiment and simulation results, the mechanism of the vertical crack formation was proposed as seen in Fig. 14, which can be largely explained in four stages. Firstly, because the Al layer was polycrystalline structure, stress induced by coefficient of thermal expansion (CTE) mismatch will concentrate at the grain boundaries of Al layer. Similar studies have been reported where the polycrystalline metallic thin film is subjected to macroscopically uniform compressive stress [33]. As a result, the grain boundary is subjected to a higher compressive stress, while the inside of the grain is subjected to a lower compressive stress. Stress gradient is generated between the grain boundary and the inside of the grain of the Al layer, leading to the hillock-like deformation during the thermal shock test as shown in Fig. 14a. Secondly, the path of the crack opens as the porous networks are partially broken in the vertical direction by this hillock as displayed in Fig. 14b. Thirdly, as Al deforms further by repeated thermal shock, the crack is completely open with the stress gradient of the sintered Ag layer. Finally, mechanical damage caused by these processes results in completely deformed interfaces and severe crack as displayed in Fig. 14c. The start of all these processes started from the interfacial deformation by Al hillock, and no vertical cracks were observed in the joint because interfacial behavior was suppressed by Ni metallization layer.

Effect of Ag atom diffusion to promote growth of Ag necking thickness

In this study, the effect of Ag atom diffusion to promote growth of Ag grain size and necking thickness was also discussed. As introduced before, the average grain size of the initial sintered Ag layer was 0.22 µm, which grew for both cases with and without the Ni metallization layer, where the average grain size was 0.45 µm and 0.57 µm, respectively. The average grain size of sintered Ag joints with the Ni metallization layer was larger than that without Ni metallization layer. Due to large deformation generated from Al layer without Ni metallization layer, some notable vertical cracks and large voids generated inside sintered Ag layer as seen in Fig. 15a. The thermal stress will concentrate to these cracks, and resulting in relatively lower stress inner the sintered Ag as the shear stress distribution shown in Fig. 13b. The relatively lower stress leads to a slow driving force for atomic diffusion. Therefore, these defects have some effects on stress distribution and thus lead to the Ag atom diffusion change to slow at the high temperature.

In addition, as the Ag diffusion cannot progress uniformly in sintered Ag layer, the recrystallization process of the Ag grain become slower in the case of joint without the Ni metallization layer than that with the Ni metallization layer. In contrast, the Ni metallization layer undergoes active recrystallization and necking thickness growth due to atomic diffusion throughout the Ag-sintered joint during thermal shock tests because there is no deformation or cracking at the Ag–Al interface as shown in the schematic diagram of Fig. 15b.

In addition, Ag-sintered joint structures were reported in previous studies during thermal aging tests at high temperatures of 250 °C. The results revealed that sintered Ag layer did not experience the vertical cracking [23, 34–37]. The microstructure of

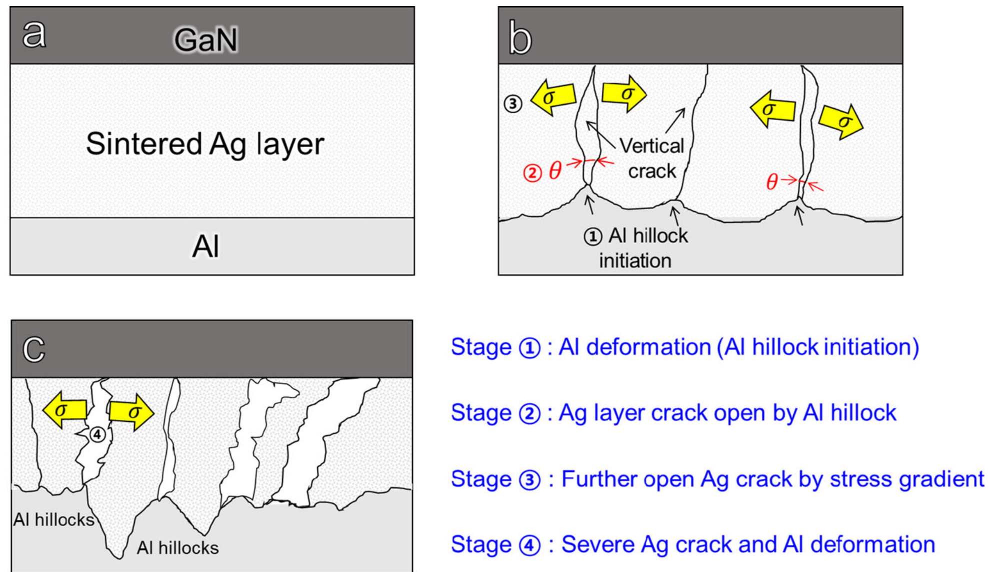

Figure 14 Vertical crack mechanism from Al hillock generation. **a** Initial state, **b** the path of the crack opens as the porous networks are partially broken in the vertical direction due to Al hillock formation, **c** completely deformed interfaces and severe crack formation.

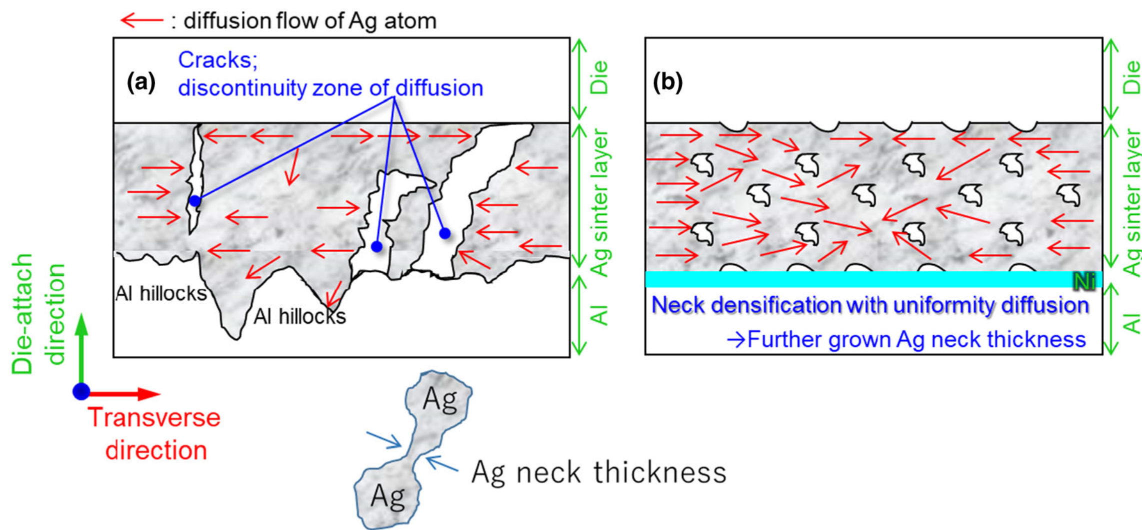

Figure 15 **a** Schematic description of the relationship between Ag atom diffusion and interface degradation and (**b**) Ag atom diffusion in the case of suppressed interface degradation.

sintered Ag layer became clearly coarsened after aging at 250 °C in air for 100 h. On the other hand, Ag-sintered joints were subjected to seriously vertical cracking with interfacial damage during the thermal shock cycling test [20, 38]. In particular, it was also found that the growth of Ag necking thickness of sintered Ag layer during the thermal shock cycling was relatively slower than that the growth during thermal aging. Therefore, vertical cracking can be suggested as interfering with the growth of Ag necking thickness by a discontinuous space formation because it prevents the Ag atom from actively diffusing inside sintered Ag layer.

Heat-resistant contribution of ultrafine-grained Ni metallization

A previous study [39] has been reported that the electro-less Ni–P coating has a fracture toughness of less than about 10 MPa·m$^{0.5}$, and electroplated fine-grain nickel has been reported as having excellent fracture toughness exceeding 53 MPa·m$^{0.5}$ [40, 41].

The sputtered nickel in this study was ultra-fine grain of 600–700 nm, and thus, it can be expected to have high fracture toughness. The Ni layer suppressed the hillock-like deformation during the thermal shock process, thereby successfully suppressing the vertical cracking of the Ag-sintered layer. Moreover, as shown in Fig. 8, since Ni sustains the same microstructure as in the initial stage even after the thermal shock test, it is expected to make a substantial contribution in the automotive industry that must guarantee a long life time in a harsh environment.

Conclusions

In summary, by sputtered 7 μm Ni with exceptional mechanical properties on DBA substrate, we succeeded in inducing pore size reduction and complete recrystallization of sintered Ag joint during harsh thermal shock tests (− 50/250 °C). This result suppressed the significant decrease in shear strength that is often observed after severe long-term thermal shock tests. The thermo-mechanical stress from the interface does not dissipate and is uniformly transferred to the sintered Ag joint layer in the case with Ni metallization layer, leading to more active recrystallization than that the die-attached structure without Ni metallization. This characteristic behavior of the grain structure for the case of the sinter Ag joints with the Ni metallization layer can be considered as evidence that the Al deformation is suppressed at the bonding interface during the thermal shock test.

The microstructure of sintered Ag layer was significantly different for the cases with and without Ni metallization because of the different thermo-mechanical stresses. It is seen that the Ag-sintered joint structure with Ni metallization layer tended to follow the typical Hall–Petch relationship by the values before and after thermal shock of 125 and 500 cycles. The grain size of Ag-sintered joint structure with Ni metallization layer may directly influence the shear strength for the Ag-sintered joint structure. In addition, the mechanisms of vertical cracking and strength reduction were numerically verified in terms of mechanics using a FEM simulation. Consequently, we found that the vertical crack formation was attributed to the propagation of the thermal and stress gradients distributed within the sintered Ag layer owing to the hillock-like deformation of the interface. Our unprecedented demonstration provides an understanding of failure mechanisms with different metallization layers that can improve the long-term reliability of Ag sinter joining technology to realize high-power density applications.

Acknowledgements

This work was supported by the JST Advanced Carbon Technology Research and Development Program (ALCA) project "Development of a high frequency GaN power module package technology" (Grant No. JPMJAL1610). This paper also is based on results obtained from a project (JPNP14004) commissioned by the New Energy and Industrial Technology Development Organization (NEDO).

Author contributions

D.K completed the sinter Ag joining, thermal shock experiments, and studies reported in this work with technical guidance from C.C, S.N and K.S. S.L and S.L provided the analysis of EBSD. The manuscript was written by D.K. with contributions from all other authors.

Data availability

The raw/processed data required to reproduce these findings cannot be shared at this time as the data also forms part of an ongoing study.

Compliance with ethical standards

Conflict of interest The authors declare that they have no known competing financial interests or personal relationships that could have appeared to influence the work reported in this paper.

Consent for publication This is to certify that the results of this paper are our original works. The data in this paper have not been published elsewhere.

References

[1] Chin HS, Cheong KY, Ismail AB (2010) A review on die attach materials for SiC-based high-temperature power

devices. Metall Mater Trans B 41:824–832. https://doi.org/10.1007/s11663-010-9365-5

[2] Chen C, Suganuma K (2019) Microstructure and mechanical properties of sintered Ag particles with flake and spherical shape from nano to micro size. Mater Des 162:311–321. https://doi.org/10.1016/j.matdes.2018.11.062

[3] Noh S, Choe C, Chen C, Suganuma K (2018) Heat-resistant die-attach with cold-rolled Ag sheet. Appl Phys Express 11(1):016501. https://doi.org/10.7567/APEX.11.016501

[4] Suganuma K, Nagao S, Sugahara T, Yokoi E, Zhang H, Jiu J (2016) Silver sinter joining and stress migration bonding for WBG die-attach. In 2016 International Symposium on 3D Power Electronics Integration and Manufacturing (3D-PEIM) vol 2, doi: https://doi.org/10.1109/3DPEIM.2016.7570554

[5] Liu X, He S, Nishikawa H (2016) Thermally stable Cu3Sn/Cu composite joint for high-temperature power device. Scr Mater 110:101–104. https://doi.org/10.1016/j.scriptamat.2015.08.011

[6] Knoerr M, Kraft S, Schletz A (2010) Reliability assessment of sintered nano-silver die attachment for power semiconductors. In 2010 12th Electronics Packaging Technology Conference. IEEE, (p 56–61) doi: https://doi.org/10.1109/EPTC.2010.5702605

[7] George E, Das D, Osterman M, Pecht M (2011) Thermal cycling reliability of lead-free high-temperature applications. IEEE Trans Device Mater Reliab 11:328–338. https://doi.org/10.1109/TDMR.2011.2134100

[8] Quintero PO, Mccluskey FP (2011) temperature cycling reliability of high-temperature lead-free die-attach technologies. IEEE Trans Device Mater Reliab 11:531–539. https://doi.org/10.1109/TDMR.2011.2140114

[9] George E, Pecht M (2016) Microelectronics reliability RoHS compliance in safety and reliability critical electronics cost reliability. Microelectron Reliab 65:1–7. https://doi.org/10.1016/j.microrel.2016.07.150

[10] Suganuma K (2001) Advances in lead-free electronics soldering. Curr Opin Solid State Mater Sci 5:55–64. https://doi.org/10.1016/S1359-0286(00)00036-X

[11] Lee J, Kim K, Suganuma K, Takenaka J, Hagio K (2005) Interfacial properties of Zn – Sn alloys as high temperature lead-free solder on Cu substrate. Mater Trans 46:2413–2418. https://doi.org/10.2320/matertrans.46.2413

[12] Kim S, Kim KS, Kim SS, Suganuma K, Izuta G (2009) Improving the reliability of Si die attachment with Zn-Sn-based high-temperature Pb-free solder using a TiN diffusion barrier. J Electron Mater 38:2668–2675. https://doi.org/10.1007/s11664-009-0928-7

[13] Gusak AM, Tu KN, Chen C (2020) Extremely rapid grain growth in scallop-type Cu6Sn5 during solid–liquid interdiffusion reactions in micro-bump solder joints. Scr Mater 179:45–48. https://doi.org/10.1016/j.scriptamat.2020.01.005

[14] Telang AU, Bieler TR, Zamiri A, Pourboghrat F (2007) Incremental recrystallization/grain growth driven by elastic strain energy release in a thermomechanically fatigued lead-free solder joint. Acta Mater 55:2265–2277. https://doi.org/10.1016/j.actamat.2006.11.023

[15] Wang S, Li M, Ji H, Wang C (2013) Rapid pressureless low-temperature sintering of Ag nanoparticles for high-power density electronic packaging. Scr Mater 69:789–792. https://doi.org/10.1016/j.scriptamat.2013.08.031

[16] Qi K, Chen X, Lu GQ (2008) Effect of interconnection area on shear strength of sintered joint with nano-silver paste. Solder Surf Mt Technol 20:8–12. https://doi.org/10.1108/09540910810861431

[17] Kim MS, Nishikawa H (2014) Silver nanoporous sheet for solid-state die attach in power device packaging. Scr Mater 92:43–46. https://doi.org/10.1016/j.scriptamat.2014.08.010

[18] Yan JJ, Zou G, Wu AP, Ren J, Yan JJ, Hu A et al (2012) Pressureless bonding process using Ag nanoparticle paste for flexible electronics packaging. Scr Mater 66:582–585. https://doi.org/10.1016/j.scriptamat.2012.01.007

[19] Milhet X, Nait-Ali A, Tandiang D, Liu YJ, Van Campen D, Caccuri V et al (2018) Evolution of the nanoporous microstructure of sintered Ag at high temperature using in-situ X-ray nanotomography. Acta Mater 156:310–317. https://doi.org/10.1016/j.actamat.2018.06.047

[20] Kim D, Chen C, Pei C, Zhang Z, Nagao S, Suetake A et al (2019) Thermal shock reliability of a GaN die-attach module on DBA substrate with Ti/Ag metallization by using micron/submicron Ag sinter paste. Jpn J Appl Phys 58(SB):15

[21] Yu F, Cui J, Zhou Z, Fang K, Johnson RW, Hamilton MC (2017) Reliability of Ag sintering for power semiconductor die attach in high-temperature applications. IEEE Trans Power Electron 32:7083–7095. https://doi.org/10.1109/TPEL.2016.2631128

[22] Fan T, Zhang H, Shang P, Li C, Chen C, Wang J et al (2018) Effect of electroplated Au layer on bonding performance of Ag pastes. J Alloys Compd 731:1280–1287. https://doi.org/10.1016/j.jallcom.2017.09.279

[23] Chen C, Suganuma K, Iwashige T, Sugiura K, Tsuruta K (2018) High-temperature reliability of sintered microporous Ag on electroplated Ag, Au, and sputtered Ag metallization substrates. J Mater Sci Mater Electron 29:1785–1797. https://doi.org/10.1007/s10854-017-8087-8

[24] Noh S, Zhang H, Suganuma K (2018) Heat-resistant microporous Ag die-attach structure for wide band-gap

power semiconductors. Materials 11:2531. https://doi.org/10.3390/ma11122531

[25] Kim D, Chen C, Noh S, Lee SJ, Zhang Z, Kimoto Y et al (2019) Development of high-strength and superior thermal shock-resistant GaN/DBA die attach structure with Ag sinter joining by thick Ni metallization. Microelectron Reliab 100–101:113380. https://doi.org/10.1016/j.microrel.2019.06.072

[26] Kim D, Chen C, Lee SJ, Nagao S, Suganuma K (2020) Strengthening of DBA substrate with Ni/Ti/Ag metallization for thermal fatigue-resistant Ag sinter joining in GaN power modules. J Mater Sci Mater Electron 31:3715–3726. https://doi.org/10.1007/s10854-020-02930-w

[27] Pei C, Chen C, Suganuma K, Fu G (2018) Thermal stability of silver paste sintering on coated copper and aluminum substrates. J Electron Mater 47:811–819. https://doi.org/10.1007/s11664-017-5857-2

[28] Chen C, Nagao S, Zhang H, Jiu J, Sugahara T, Suganuma K, Iwashige T, Sugiura K, Tsuruta K (2017) Mechanical deformation of sintered porous Ag die attach at high temperature and its size effect for wide-bandgap power device design. J Electron Mater 46:1576–1586. https://doi.org/10.1007/s11664-016-5200-3

[29] Chen C, Choe C, Kim D, Suganuma K (2020) Life time prediction of SiC power module by micron/submicron Ag sinter joining based on fatigue, creep and thermal properties from room temperature to high temperature. J Electron Mater. https://doi.org/10.1007/s11664-020-08410-5

[30] Shen TD, Schwarz RB, Feng S, Swadener JG, Huang JY, Tang M et al (2007) Effect of solute segregation on the strength of nanocrystalline alloys: inverse hall-petch relation. Acta Mater 55:5007–5013. https://doi.org/10.1016/j.actamat.2007.05.018

[31] Thompson AW, Baskes MI, Flanagan WF (1973) The dependence of polycrystal work hardening on grain size. Acta Metall 21:1017–1028. https://doi.org/10.1016/0001-6160(73)90158-2

[32] Chen C, Nagao S, Suganuma K, Jiu J, Sugahara T, Zhang H et al (2017) Macroscale and microscale fracture toughness of microporous sintered Ag for applications in power electronic devices. Acta Mater 129:41–51. https://doi.org/10.1016/j.actamat.2017.02.065

[33] Ri S, Saka M (2012) Diffusion–fatigue interaction effect on hillock formation in aluminum thin films under thermal cycle testing. Mater Lett 79:139–141. https://doi.org/10.1016/j.matlet.2012.03.109

[34] Kim D, Chen C, Nagao S, Suganuma K (2020) Mechanical characteristics and fracture behavior of GaN/DBA die-attached during thermal aging: pressure-less hybrid Ag sinter joint and Pb–5Sn solder joint. J Mater Sci Mater Electron 31:587–598. https://doi.org/10.1007/s10854-019-02563-8

[35] Zhang Z, Chen C, Wu AT, Suganuma K (2019) Improvement of high-temperature thermal aging reliability of Ag–Au joints by modifying Ni/Au surface finish. J Mater Sci Mater Electron 30:20292–20301. https://doi.org/10.1007/s10854-019-02415-5

[36] Chen C, Choe C, Kim D, Zhang Z, Long X, Zhou Z et al (2020) Effect of oxygen on microstructural coarsening behaviors and mechanical properties of Ag sinter paste during high-temperature storage from macro to micro. J Alloys Compd 834:155173. https://doi.org/10.1016/j.jallcom.2020.155173

[37] Chen C, Zhang Z, Wang Q, Zhang B, Gao Y, Sasamura T et al (2020) Robust bonding and thermal-stable Ag–Au joint on ENEPIG substrate by micron-scale sinter Ag joining in low temperature pressure-less. J Alloys Compd 828:154397. https://doi.org/10.1016/j.jallcom.2020.154397

[38] Kim D, Chen C, Suetake A, Choe C, Sugahara T, Nagao S et al (2018) Development of thermal shock-resistant of GaN/DBC die-attached module by using Ag sinter paste and thermal stress relaxation structure. Microelectron Reliab 88–90:779–787. https://doi.org/10.1016/j.microrel.2018.07.044

[39] Shen YF, Xue WY, Liu ZY, Zuo L (2010) Nanoscratching deformation and fracture toughness of electroless Ni-P coatings. Surf Coatings Technol 205:632–640. https://doi.org/10.1016/j.surfcoat.2010.07.066

[40] Dai W, Oropeza C, Lian K, Wang W (2006) Experiment design and UV-LIGA microfabrication technology to study the fracture toughness of Ni microstructures. Microsyst Technol 12:306–314. https://doi.org/10.1007/s00542-005-0056-0

[41] Chen J, Bull SJ (2009) Finite element analysis of contact induced adhesion failure in multilayer coatings with weak interfaces. Thin Solid Films 517:3704–3711. https://doi.org/10.1016/j.tsf.2009.02.121

Publisher's Note Springer Nature remains neutral with regard to jurisdictional claims in published maps and institutional affiliations.